Chemometrics and Intelligent Laboratory Systems 184 (2019) 112–122

Contents lists available at ScienceDirect

Chemometrics and Intelligent Laboratory Systems

journal homepage: www.elsevier.com/locate/chemometrics

Supervised classification of monomodal and multimodal hyperspectral data in vibrational microspectroscopy: A comprehensive comparison

Ch. Pomrehn [a,*], D. Klein [b], A. Kolb [c], P. Kaul [b], R. Herpers [a,d,e]

[a] Institute of Visual Computing, Hochschule Bonn-Rhein-Sieg University of Applied Sciences, Grantham-Alle 20, 53757, Sankt Augustin, Germany
[b] Institute of Safety and Security Research, Hochschule Bonn-Rhein-Sieg University of Applied Sciences, Von-Liebig-Str. 20, 53359, Rheinbach, Germany
[c] Institute for Vision and Graphics, University of Siegen, Hölderlinstr. 3, 57076, Siegen, Germany
[d] Faculty of Computer Science, University of New Brunswick, 550 Windsor St., Fredericton, Canada
[e] Lassonde School of Engineering, York University, 4700, Keele St., North York, Canada

ARTICLE INFO

Keywords:
Supervised classification
Pattern recognition
Multimodal hyperspectral data
Vibrational microspectroscopy
Chemical imaging

ABSTRACT

The application of Raman and infrared (IR) microspectroscopy is leading to hyperspectral data containing complementary information concerning the molecular composition of a sample. The classification of hyperspectral data from the individual spectroscopic approaches is already state-of-the-art in several fields of research. However, more complex structured samples and difficult measuring conditions might affect the accuracy of classification results negatively and could make a successful classification of the sample components challenging. This contribution presents a comprehensive comparison in supervised pixel classification of hyperspectral microscopic images, proving that a combined approach of Raman and IR microspectroscopy has a high potential to improve classification rates by a meaningful extension of the feature space. It shows that the complementary information in spatially co-registered hyperspectral images of polymer samples can be accessed using different feature extraction methods and, once fused on the feature-level, is in general more accurately classifiable in a pattern recognition task than the corresponding classification results for data derived from the individual spectroscopic approaches.

1. Introduction

The comprehensive term *vibrational spectroscopy* summarizes a number of optical measuring concepts that are applied to analyze the molecular structure and composition of a sample [18]. They are widely used in several fields of research such as analytical chemistry [13], pharmaceutical analysis [8], food sciences [27], biomedical applications and diagnostics [7,20], as well as in material sciences [10]. The most important of the applied methods are Raman and IR spectroscopy. Both concepts are based on the interaction between electromagnetic radiation and molecular vibrations resp. rotations. From this interaction, material-specific spectral *fingerprints* can be derived, providing information that enables the identification and the qualitative or quantitative analysis of samples [18,19]. Although both methods share an underlying principle, they differ in terms of the demands concerning their physical processes, leading to the *rule of mutual exclusion* [26], which defines that vibrations and rotations that are active for Raman spectroscopy are non-active for IR spectroscopy, and vice versa. Hence, both concepts can generally be considered as complementary methods [18,19]. Consequently, a combined consideration of Raman and IR spectroscopic measurements should lead to an improved potential for solving challenging analytical problems in vibrational spectroscopic analysis.

The application of vibrational spectroscopic measurements on a microscopic level is realized by combining Raman and IR spectroscopy with conventional brightfield microscopic systems. In *vibrational microspectroscopy*, point-wise measurements are usually performed in a grid-pattern on a sample, leading to microscopic hyperspectral images. In comparison to standard *RGB* images, these complex data structures provide hundreds or even thousands of channels often denoted as spectral bands. The concept of creating maps that provide both, spectral information and its spatial distribution, is termed chemical imaging (CI) [22]. In many cases, dimensionality reduction (DR) methods are applied to introduce a class-representative visualization of the chemical image, derived from unsupervised or supervised classification in a pattern recognition task. Hence, supervised and unsupervised classification of hyperspectral images is of major interest in the field of applied

* Corresponding author.
E-mail address: christoph.pomrehn@h-brs.de (Ch. Pomrehn).

https://doi.org/10.1016/j.chemolab.2018.11.013
Received 5 June 2018; Received in revised form 6 November 2018; Accepted 19 November 2018
Available online 28 November 2018

microspectroscopy.

But even though the complementary nature of Raman and IR methods is well known and combined approaches are explicitly demanded [12], most of the publications deal with comparative studies [12,14–16]. Prior work and publications that deal with fused data from both spectroscopic approaches are rare. In Ref. [5], F. Clark et al. used a device-based registration concept and univariate visualization methods to provide co-registered chemical images of pharmaceutical components. Their approach of chemical image fusion based on color composition, improves the available spectral information, resulting in a complete visualization of the chemical composition of pharmaceutical blends. D. Perez-Guaita et al. [24] applied multivariate analysis on co-registered images of cells, achieving valuable information concerning the cell composition. In Ref. [9], A. Gowen and R. M. Dorrepal investigated the potential of multivariate data fusion in vibrational spectroscopy for supervised single pixel classification, using a polymer sample. Here, especially the data fusion on the feature level led to improved classification rates. However, methods of feature extraction were limited to PCA, and supervised classification only considered partial least square discriminant analysis (PLS-DA). Furthermore, the polymer sample only contains 2 different components, leading to a 3-class classification problem of pure material targets.

In this contribution, we build on the results from Gowen and Dorrepal in Ref. [9] by a more extensive comparison between supervised classification results of single and fused data sets generated by Raman and IR microspectroscopic measurements. Co-registered hyperspectral images were generated via rasters of point measurements for two polymer samples, leading to hyperspectral data that is assignable to 7 different classes of pure and mixed material distributions. The purpose of this contribution is to support the hypothesis, that the fusion of complementary data from both measurement concepts leads to a more accurate classification of the complex hyperspectral signatures of two polymer samples, in comparison to data generated by the individual spectroscopic approaches. Since results of supervised classification depend significantly on the choice of the classifier, the selected features and their dimensionality, and on the used training data, a high number of individual classification setups that differ in the composition of these components was investigated in independent classification processes. This research shows that the use of spectral features fused on the feature level improves classification rates of supervised classifiers for a clear majority of the considered classification setups.

The rest of this contribution is organized as follows: In Section 2, the experimental background of this investigation is presented and the terms *multimodal* and *monomodal*, as they are used within the scope of this contribution, are defined. We furthermore present the mathematical concept of the used dimensionality reduction techniques and supervised classifiers in Section 3. Results and discussion in Section 4 are followed by the conclusion in Section 5. Detailed results of individual classification setups are given in Table 1 and Table 2.

2. Experimental design

2.1. Classification of monomodal and multimodal data

The objective of this investigation was to support the hypothesis that hyperspectral images derived from Raman and IR microspectroscopy contain complementary information that improves the classification of complex material-specific spectral signatures and that is accessible by statistic-based dimensionality reduction techniques, which are established in the field of hyperspectral data processing. To verify the assumptions, supervised classification of multimodal and monomodal data was implemented. With monomodal data, we denote data that was generate from one of the individual microspectroscopic approaches and that has not been further fused with other data. Thus, monomodal data contains spectral information that is subject to the selection rules of the individual microspectroscopic concept. In accordance with this definition, approaches, images and feature vectors that consider or contain data derived from a single spectroscopic method are also denoted as monomodal. By multimodal data, we mean data that was computed by the fusion of monomodal data. Thus, multimodal data contains spectral information from both microspectroscopic approaches. In accordance with this definition that refers to [17], approaches, images and feature vectors that consider or contain multimodal data are denoted as multimodal as well, like it was already done in Ref. [24]. According to the general procedure presented in Fig. 1, hyperspectral images of microscopic polymer samples were acquired using IR and Raman microspectroscopic devices. The hyperspectral images can be segmented into areas of seven different classes, providing spectral signatures of pure and mixed material distributions. To ensure that pixel vectors in both images are generated at points with spatial correspondence, a device-based registration was implemented. After preprocessing, to separate relevant and redundant spectral information, different dimensionality reduction techniques were individually applied on the co-registered images according to the considered classification setup. For each spectroscopic method, a variety of monomodal feature vectors was computed. Multimodal feature vectors were generated by a concatenation of monomodal feature vectors and can therefore be considered as fused on the feature level. The evaluation was focused on a comparison of the classification rates for the classification of monomodal and multimodal data.

We expected the advantage of a multimodal approach to be reflected in improved classification rates for a high number of different classification setups, in comparison to the corresponding setups in monomodal approaches. We therefore considered two different supervised classification scenarios. In the first scenario, the original data sets were split into training and test data sets by sub-sampling. Thus, training and test data can be considered as data sets from two different measurements of the same sample. Features derived by dimensionality reduction methods from the training data sets were used to train the classification models in a 5-fold cross validation training procedure. Subsequently, the test data sets were projected into the feature space derived from the training data sets and were used for further validation. In the second scenario, the data sets were considered as sets of single measurements that can be subdivided into few spectral signatures of known class affiliation and a majority of unknown class membership. Here, the original data set was transformed to the feature spaces by dimensionality reduction methods. Training data sets were created by randomly selecting feature vectors of each class from the transformed data. It was further ensured that the training data sets have the same number of feature vectors for each class. To create the test data sets, each feature vector used within the training procedure was removed from the transformed original data. Thus, a separation of training and test data sets was ensured while their mutual influence was restricted to the common dimensionality reduction transform. The training data sets were used to train the considered classification models in a 5-fold cross validation training procedure. Further validation was performed using the generated test data sets. Since the results of the trained model depend on the chosen training vectors, in particular for small training data sets, this scenario was performed over 100 runs for each classification setup. The results are presented as averaged classification rates.

The use of microscopic polymer samples that show classes of pure and mixed material distributions meant that the complexity of the spectral data and the difficulty of its classification was increased in relation to [9]. The increase in complexity should emphasize the potential of a multimodal microspectroscopic approach, especially in the context of challenging pattern recognition tasks. The high variety concerning the choice of features and classifiers, as well as the varying dimensionality of the feature space and the composition of the training data that were considered in the individual classification procedures, should further underline the general benefit of this concept and its independence from specific classification setup. Therefore, classification rates and their distribution concerning the degree of improvement were evaluated for all setups. To make more specific statements regarding the results of single

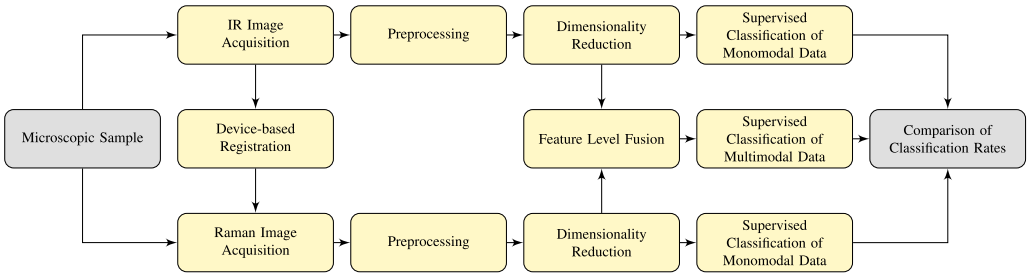

Fig. 1. General procedure of the individual comparison of classification results for multimodal and monomodal data derived from co-registered hyperspectral images generated by Raman and IR microspectroscopy.

sample components, a class-dependent evaluation of the results was also performed. Furthermore, the plausibility of the extension of the feature space was examined exemplarily.

2.2. Sample preparation

A prerequisite for preparing a microscopic sample used in a multimodal approach is the activity of its components with respect to both microspectroscopic approaches. Furthermore, it should be possible to distribute the chosen substances on a microscopic scale, so that sufficiently strong measuring signals can be obtained. The complex molecular structure of polymers has proven to be sufficiently active for both approaches [12]. Additionally, their use in a dissolved state allows a proper sample preparation. For a comprehensive comparison of classification rates, two microscopic samples consisting of different transparent polymers and a synthetic colorant were prepared on a gold mirror. The first polymer sample (PS1) consisted of polymethylmethacrylat (PMMA), styrene-acrylonitrile (SAN) and the black colorant of a flow pen. For the second polymer sample (PS2), polystyrene (PS), PMMA and polyetherimide (PEI) were used. All polymers were placed in a dissolved state and dried under a fume hood. Both samples provided areas of pure material distributions, as well as regions of mixed material distributions. Consequently, the test items consisted of multi, pure and mixed material targets that were classified.

2.3. Image acquisition

Hyperspectral data sets were generated using the Raman system *Senterra* and the IR microscopic system *Hyperion 3000* in combination with the *Vertex 70* spectrometer, all developed by the *Bruker Cooperation*. To ensure a co-registration of the generated data, a device-based registration procedure in analogy to [5] was implemented. Here, concentric-ring fiducial markers were manufactured on a microscope slide via electron beam lithography and located by a computer vision-based approach as reference positions. A rigid transformation derived from the reference positions, located for each system, was applied to adjust the measuring position grid for the different spectroscopic approaches. Before measurements were initiated, the determined measuring grids were reviewed and manually adjusted, if necessary. In both systems, 70×70 raster measurements were applied on both samples, leading to hyperspectral images with an equivalent pixel resolution. For the Raman measurements, PS1 was excited by a 785 *nm* wavelength laser of 10 *mW* power. The data was acquired over an integration time of 2 s over 2 accumulations per point measurement. Signal amounts were collected in a spectral range of 410–1790 cm^{-1} with a spectral resolution of 0.5 cm^{-1}. PS2 was excited by a 785 *nm* wavelength laser of 100 *mW* power. An integration time of 2 s over 2 accumulations was used per point measurement. Here, signal amounts were collected in a spectral range of 50–1520 cm^{-1} with a spectral resolution of 0.5 cm^{-1}. The corresponding IR measurements were carried out in reflectance mode, in a spectral range of 600–4000 cm^{-1} and a spectral resolution of 2 cm^{-1} for both samples. Here, five scans per point measurement were used for PS1. For PS2, the number of scans was further reduced to a single one.

2.4. Preprocessing

The 4900 raw spectra of each hyperspectral image were preprocessed according to state-of-the-art procedures for hyperspectral data in vibrational microspectroscopy [25]. The preprocessing pipeline includes outlier control, vector normalization, baseline correction and data smoothing. Furthermore, all preprocessed spectra were sub-sampled and cropped to a relevant wavenumber range. More precisely, Raman spectra of PS1 were cropped to a wavenumber range of 410–1490 cm^{-1}. The corresponding IR spectra were cropped to a spectral range of 600–3230 cm^{-1}. For PS2, the wavenumber range of the Raman dataset was constrained to 150–1520 cm^{-1} and to 600–3300 cm^{-1} for the IR data. All spectra were normalized to a range of 0–1 by min-max normalization. Baseline correction was performed using an asymmetric least square (asLS) approach [23], where regularization parameters were chosen to be $\lambda = 10^6$ and $p = 10^{-3}$, with a maximum of 50 iterations and a termination criterion of $\varepsilon = 10^{-6}$. All spectra were additionally smoothed by local kernel regression using locally weighted scatter-plot smoothing (LOESS) [6]. All preprocessing methods were performed in MATLAB. We used the MATLAB Curve Fitting Toolbox for spectral smoothing by local kernel regression. A baseline correction code based on asLS was provided by Peng et al. in Ref. [23].

3. Dimensionality reduction and supervised classification

Established component analysis transformations based on second-order statistics and a feature extraction transformation have been used. Namely, variance-based principal component analysis (PCA) [4] and signal-to-noise ratio (SNR)-based maximum noise fraction (MNF) [4] have been applied. Furthermore, Fisher's linear discriminant analysis (FLDA) [2], which can be seen as a feature extraction transformation and supervised classifier, was considered. Additionally, further supervised classification approaches based on statistical learning theory were specified: Support Vector Machine (SVM) and Naive Bayes Classifier (NBC). We refer to the notation and mathematical description of C.—I. Chang [4], C. Aggarwal [1] and C. Bishop [2].

3.1. Principal component analysis

PCA purposes a dimensionality reduction of a high-dimensional data set, while retaining as much as possible of its variation. It determines a set of uncorrelated linear functions of the elements of the data set having maximum variance [11]. Defining $\boldsymbol{X}$ as the data sample matrix with $\boldsymbol{X} = [\boldsymbol{r}_1 \boldsymbol{r}_2 \ldots \boldsymbol{r}_N]$ and $\boldsymbol{\mu}$ as the mean of all L-dimensional hyperspectral pixel vectors, the covariance matrix $\boldsymbol{K}$ of the mean-centered original data matrix $\boldsymbol{X}'$ can be determined by

$$\boldsymbol{K} = \frac{1}{N}\left[\boldsymbol{X}'\boldsymbol{X}'^{T}\right] = \frac{1}{N}\left[\sum_{i=1}^{N}(\boldsymbol{r}_i - \boldsymbol{\mu})(\boldsymbol{r}_i - \boldsymbol{\mu})^T\right]. \quad (1)$$

Using an eigendecomposition, the eigenvalues of **K** and a matrix $\boldsymbol{\Lambda} = [\boldsymbol{v}_1, \boldsymbol{v}_2 \ldots \boldsymbol{v}_L]$ of the corresponding eigenvectors can be determined. Defining a linear transformation $\xi_\Lambda(\boldsymbol{r}) = \boldsymbol{\Lambda}^T \boldsymbol{r}$ denoted as principal component transform, the data sample matrix can be transformed into a new de-correlated matrix $\tilde{\boldsymbol{X}}$. The l-th component of $\tilde{\boldsymbol{X}}$ is obtained by $\xi_{\boldsymbol{v}_l}(\boldsymbol{X}') = \boldsymbol{v}_l^T \boldsymbol{X}'$ and is called the l-th principal component. By applying the transform ξ_Λ to each sample of $\boldsymbol{X}'$, a set of all principal components is determined. However, for dimensionality reduction, only those eigenvectors are considered that correspond to the largest eigenvalues, and thus provide the principal components with highest variance [4,11].

3.2. Maximum noise fraction

MNF purposes to determine a set of new components that are ordered in terms of the image quality of the hyperspectral band images. For that, the l-th hyperspectral band image of size $N = n_r n_c$ can be represented as a column observation vector of dimensionality N with $\boldsymbol{b}_l = (r_{l1}, r_{l2}, \ldots, r_{lN})$. Let $\boldsymbol{s}_l$ and $\boldsymbol{n}_l$ be the corresponding signal and uncorrelated noise vector, the observation model is given by $\boldsymbol{b}_l = \boldsymbol{s}_l + \boldsymbol{n}_l$. Assuming the noise variance to be $\sigma^2_{\boldsymbol{n}l}$ and the observation variance to be $\sigma^2_{\boldsymbol{b}l}$, the noise fraction (NF) of the l-th hyperspectral band image vector can be defined by $NF_l = \sigma^2_{\boldsymbol{n}_l} / \sigma^2_{\boldsymbol{b}_l}$. MNF finds the transformation $\boldsymbol{w}_l^{MNF}$ that maximizes NF_l:

$$max_{wl}\left\{\sigma^2_{\boldsymbol{n}_l} \Big/ \sigma^2_{\boldsymbol{b}_l}\right\} = max_{\boldsymbol{w}_l}\left\{\frac{\boldsymbol{w}_l^T \left[\sigma^2_{\boldsymbol{n}_l}\right] \boldsymbol{w}_l}{\boldsymbol{w}_l^T \left[\sigma^2_{\boldsymbol{b}_l}\right] \boldsymbol{w}_l}\right\} = \frac{\left(\boldsymbol{w}_l^{MNF}\right)^T \left[\sigma^2_{\boldsymbol{n}_l}\right] \boldsymbol{w}_l^{MNF}}{\left(\boldsymbol{w}_l^{MNF}\right)^T \left[\sigma^2_{\boldsymbol{b}_l}\right] \boldsymbol{w}_l^{MNF}}. \tag{2}$$

The transformed band images are then ordered descendingly according to their MNF.

3.3. Fisher's linear discriminant analysis

FLDA can be used for supervised dimensionality reduction or supervised classification. Its main purpose is to find a linear combination of the labeled input data, such that the within-class variance is minimized and the between-class variance is maximized [2]. From a training vector set, the within-class scatter matrix $\boldsymbol{S}_W$ and the between-class scatter matrix $\boldsymbol{S}_B$ can be determined, considering all given classes. The generalized Fisher's ratio [2] is

$$J(\boldsymbol{W}) = Tr\left\{\left(\boldsymbol{W}^T \boldsymbol{S}_W \boldsymbol{W}\right)^{-1} \boldsymbol{W}^T \boldsymbol{S}_B \boldsymbol{W}\right\}. \tag{3}$$

The purpose of FLDA is to successively find a set of orthogonal feature vectors represented in the matrix $\boldsymbol{W}$ that maximizes Fisher's ration defined in 3 and that specifies the classification boundaries among the p classes. If the p class specific centroids of our L-dimensional input space are considered, it is noticeable that they lie in an affine subspace of dimensionality $\leq (p-1)$ [2]. If now the dimensionality L of the input data is much larger than the number of different classes p, which is normally the case with hyperspectral data, a significant DR can be achieved by projecting it to this subspace. Consequently, FLDA can also be applied as a technique for DR.

3.4. Support Vector Machine

Even though an SVM is normally considered as a binary classifier, its concept can be extended for an application in multiclass classification problems, e.g. using a set of binary classifiers in a one-vs.-one strategy. However, for presenting the general concept of the SVM principle, the mathematical background for a binary SVM is considered. We assume a linear discriminant function $y = g(\boldsymbol{r}) = \boldsymbol{w}^T \boldsymbol{r} + b$. Let $\boldsymbol{w}$ be a weighting vector, $\boldsymbol{r}$ the sample data vector and b a constant bias. Assuming a set of training data $\{(\boldsymbol{r}_i, d_i)\}_{i=1}^n$, containing the training vectors $\boldsymbol{r}_i$ and the corresponding binary decisions $\boldsymbol{d}_i$, then an SVM finds a weighting vector $\boldsymbol{w}$ and bias b such that

$$d_i = \begin{cases} 1; & \text{if } y_i = g(\boldsymbol{r}_i) = \boldsymbol{w}^T \boldsymbol{r}_i + b \geq 0) \\ -1; & \text{if } y_i = g(\boldsymbol{r}_i) = \boldsymbol{w}^T \boldsymbol{r}_i + b < 0) \end{cases} \tag{4}$$

and such that a margin, defined as distance ρ between the discrimination function and the closest training vectors of both classes, is maximized. It can be shown that this distance is defined by $\rho = 2/\|\boldsymbol{w}\|$ with $\boldsymbol{w}$ being a normal vector of the hyperplane. This maximization is equivalent to finding a weight vector $\boldsymbol{w}^*$ that minimizes

$$\Phi(\boldsymbol{w}) = (1/2)\boldsymbol{w}^T \boldsymbol{w} = (1/2)\|\boldsymbol{w}\|^2 \tag{5}$$

subjected to 4 [4]. Those vectors $\boldsymbol{r}_i$ of the training data that satisfy the equality part of 4, are denoted as support vectors.

3.5. Naive Bayes Classifier

An NBC is a probabilistic classifier based on the well-known Bayes' theorem while considering a *"naive"* independence assumption of the sample data [1]. Defining a set of training vectors $\{(\boldsymbol{r}_i, d_i)\}_{i=1}^n$, where $\boldsymbol{r}_i$ are the L-dimensional training vectors and $\boldsymbol{d}_i$ the corresponding decision labels, and assuming two random variables $\boldsymbol{X}$ and Y, where Y is a discrete class variable from the set of possible classes $\{C_i\}_{i=1}^p$ and $\boldsymbol{X}$ is feature variable with its components $X_1, \ldots, X_L$ from a training sample vector $\boldsymbol{r}_i$, one is interested in the posteriori probability $p(Y|\boldsymbol{X})$, given by Bayes' theorem as

$$p(Y|\boldsymbol{X}) = \frac{p(\boldsymbol{X}|Y)p(Y)}{p(\boldsymbol{X})} \tag{6}$$

$$p(C_i|X_1, X_2, \ldots X_L) = \frac{p(X_1, X_2, \ldots X_L|C_i)p(C_i)}{p(X_1, X_2, \ldots X_L)} \tag{7}$$

The dimensionality of $\boldsymbol{X}$ and the variability of Y significantly increase the sample complexity for the training process and make an exact learning of the classifier impractical. Thus, an independence assumption is made, assuming that, for a given Y, all considered features $X_1, X_2, \ldots X_L$ are conditionally independent of each other. Hence,

$$p(X_1, X_2, \ldots X_L|C_i) = \prod_{j=1}^L p(X_j|Ci) \tag{8}$$

which significantly decreases the number of parameters that have to be estimated. By using 8 in 7 one obtains

$$p(C_i|X_1, X_2, \ldots X_L) = \frac{\prod_{j=1}^L p(X_j|Ci)p(C_i)}{p(X_1, X_2, \ldots X_L)}. \tag{9}$$

Looking now for the most probable value of Y leads to the Naive Bayes classification rule

$$Y \leftarrow \arg\max_{C_i} p(C_i) \prod_{j=1}^L p(X_j|Ci) \tag{10}$$

4. Results and discussion

4.1. Image acquisition and reference image estimation

Co-registered hyperspectral image data sets of PS1 and PS2 were acquired using the available microspectroscopic devices. Thereby, rasters of 70 × 70 point measurements were applied according to the aforementioned parameters, leading to hyperspectral images of the regions of interest presented in Fig. 2a and e, with a corresponding pixel resolution. To ensure an accurate co-registration of the images, a device-based registration procedure as described in Section 2.3 was employed between the individual microspectroscopic measurements. As presented in Fig. 2b and f, the application of different preprocessing steps, including outlier removal, normalization, baseline removal and smoothing, resulted in two accurately co-registered image data sets providing sufficiently

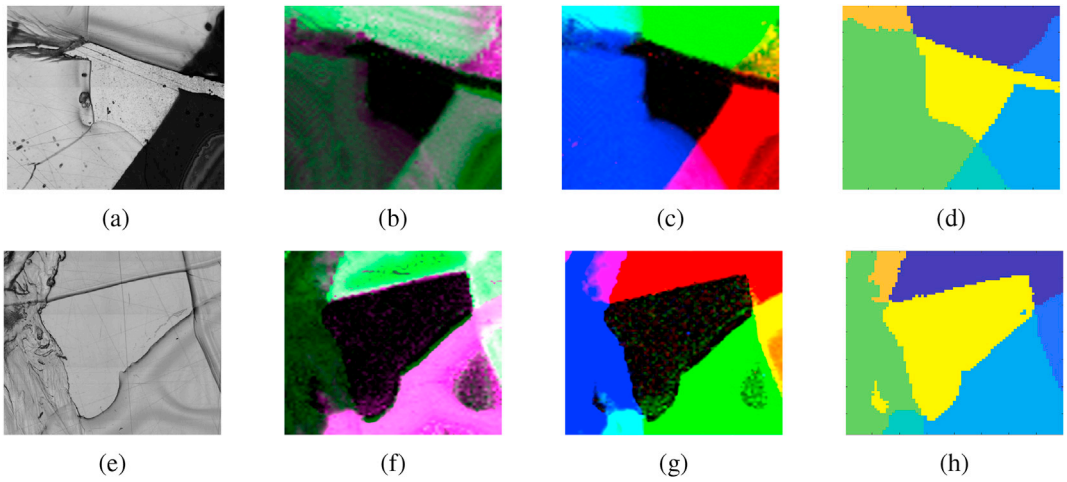

Fig. 2. Microscopic brightfield images of regions of interest for PS1 (a) and PS2 (e) and corresponding difference images (b) and (f) from univariate visualizations representing the Raman image (green) and the IR image (magenta), showing a sufficient registration accuracy of approx. ± 1.5 pixel. (c) Additive multimodal *RGB*-image from univariate visualization of PS1, consisting of PMMA (blue), SAN (green) and a black colorant (red). (d) 7-class reference image derived by manual color segmentation of (c) in the *HSI* color space. Class assignments: 1 (purple - SAN), 2 (dark blue - colorant/SAN), 3 (bright blue - colorant), 4 (cyan - colorant/PMMA), 5 (green - PMMA), 6 (orange - PMMA/SAN), 7 (yellow - background). (g) Additive multimodal *RGB* image from univariate visualization of PS2, consisting of PEI (blue), PMMA (red) and PS (green). (h) 7-class reference image derived by a manual color segmentation of (g) in the *HSI* color space. Class assignments: 1 (purple - PMMA), 2 (dark blue - PMMA/PS), 3 (bright blue - PS), 4 (cyan - PS/PEI), 5 (green - PEI), 6 (orange - PEI/PMMA), 7 (yellow - background). Note that all images have been scaled for better visualization. (For interpretation of the references to color in this figure legend, the reader is referred to the Web version of this article.)

strong signal amounts for each sample component. In these composite false-color images, signal amounts shown in magenta represent a univariate visualization derived from the Raman data while signal amounts shown in green denote the visualization derived from the IR data. Due to the different spatial resolution of both microspectroscopic concepts, a registration accuracy of approximately up to ±1.5 pixel was achieved, determined manually at four prominent points of the polymer samples.

A material specific visualization of PS1 and PS2 could be realized by univariate visualization methods. For that, signal amounts were determined by a spectral intensity integration of material specific peaks. The three different signal amounts were assigned to the channels of *RGB*-images, leading to color-encoded visualizations of the different sample components. To ensure the consideration of data from both spectroscopic approaches in a common visualization, we generated additive multimodal *RGB*-images. As shown in Fig. 2c and g, these images enable sufficient discrimination between pure and mixed material distributions. This visualization was used to create labeled reference images of 7 classes for both data sets, applying a manual color segmentation in the *HSI* color space and considering spatial information from the corresponding brightfield images. Considering Fig. 2a and e, segments of different surface texture and topologies are noticeable, which usually affect the microspectroscopic measurements. In combination with the complex spectral signatures of the mixed material distributions, the classification of the sample components as labeled according to the reference image in Fig. 2d and h, is considered as a challenging classification task.

4.2. Classification study

The use of complementary information from microspectroscopic data was investigated in classification tasks by comparing classification rates for monomodal and multimodal data of PS1 and PS2. DR and feature extraction transformation were applied to the preprocessed data. For the multimodal approach, data fusion was performed on the feature level by concatenating the individual extracted monomodal feature vectors to a new feature vector of higher dimensionality. A variety of different setups of supervised classifiers and features were considered. Since supervised classification is influenced by the composition of the training data, the training vector sets applied in the learning procedure were further varied.

Assuming that the relevant spectral information contained in a hyperspectral data cube with spectral dimension M is contained in the first $N \ll M$ dimensions of its computed feature representation, we limited the number of selected features and thereby the dimension of the feature space considered within the individual classification approaches. More specifically, the monomodal feature vectors used consisted of the first $N = 3$ (PCA3), $N = 5$ (PCA5) and $N = 10$ (PCA10) principal components, the first $N = 10$ (MNF10), $N = 20$ (MNF20) and $N = 30$ (MNF30) bands of minimum noise fraction as well as the first $N = 2$ (LDA2), $N = 4$ (LDA4) and $N = 6$ (LDA6) features derived by LDA. The generation of the training data sets was either implemented by sub-sampling the data matrix with sub-sampling factors of 2 (Sub2) and 5 (Sub5) or by randomly selecting sets of 5 (Rand5), 15 (Rand15), 25 (Rand25), 35 (Rand35) and 45 (Rand45) feature vectors per class. In the latter case, an equal class distribution was ensured, and results were presented as averaged values derived from 100 classification runs per set.

Overall, 189 different setups that combined classifier, features and training vector sets were investigated. DR by MNF and LDA were carried out using the MATLAB code provided in Refs. [3,21]. Principal components analysis and supervised classification were realized using methods from MATLAB Statistics and the Machine Learning Toolbox. The training accuracy of the supervised classifiers was evaluated using 5-fold cross validation. For classification via SVM, a multiclass model was generated using a one-versus-one training procedure. In Fig. 3a, the results of the evaluation of all individual classification setups are shown as a distribution of the highest classification rate that was found concerning a comparison of classification rates for multimodal and monomodal data.

For PS1, the multimodal approach showed that a clear majority of 97.4% and 96.8% among all classification setups resulted in a numerical improvement in classification rates and training accuracies, respectively. In those cases, the mean percentage improvement compared to the IR method was about 7.4 ± 0.7% for classification rates and 7.0 ± 0.6% for training accuracies, with a 95% confidence interval, as presented in Fig. 3b. In comparison to the Raman method, the classification rate increased by 8.4 ± 1% and training accuracy by 6.9 ± 0.8%, on average. Only in a few cases were higher classification accuracies found for monomodal IR (0.5%) or Raman (2.1%) data. Comparable results were found for PS2. Here, 90.5% and 94.2%, of all classification setups led to a numerical improvement in classification rates and training accuracies,

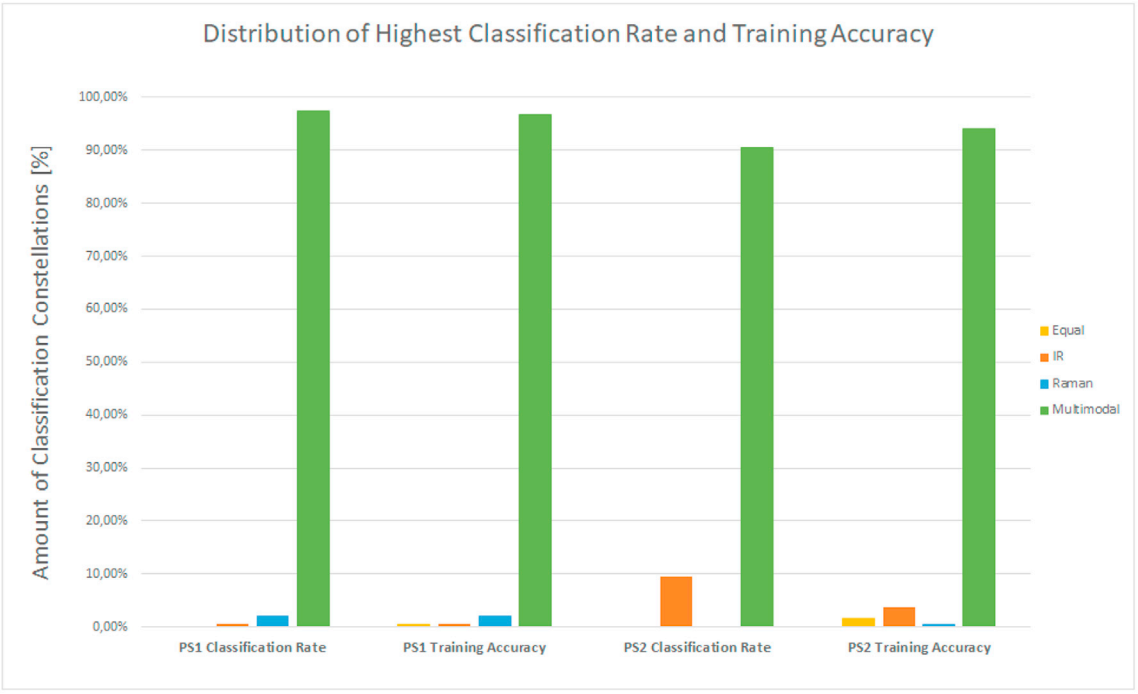

(a)

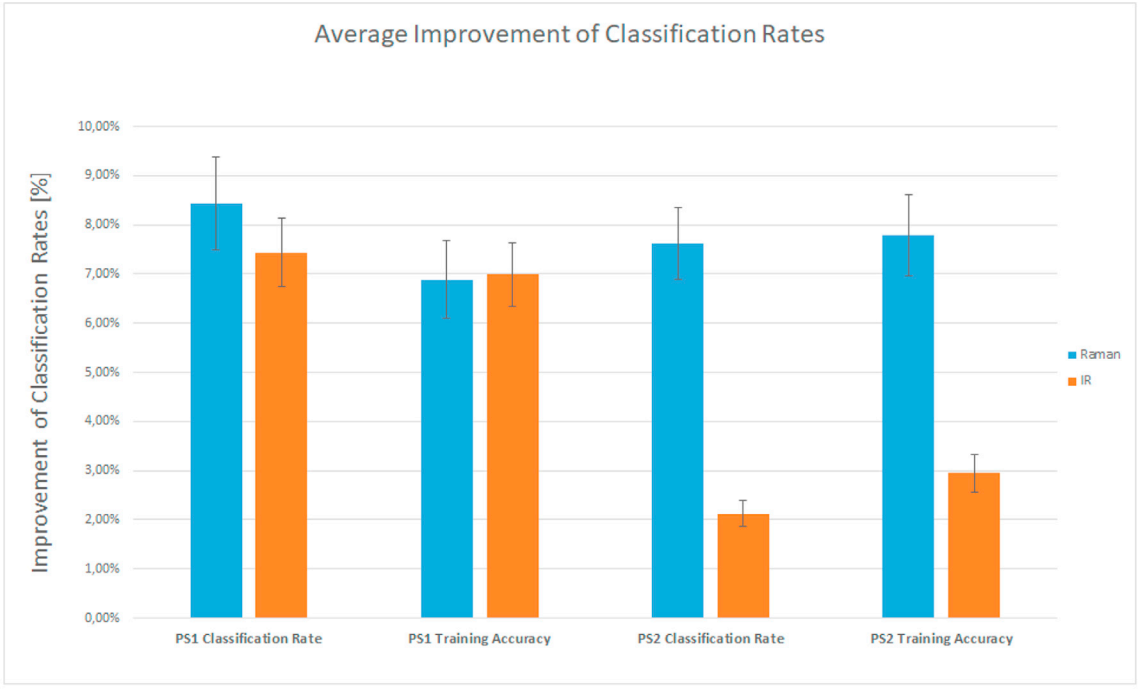

(b)

Fig. 3. (a) Distribution of highest classification rate and training accuracy for PS1 and PS2 considering all classification setups. Percentage of improved classification rates by multimodal approach (green), percentage of highest classification rate for monomodal IR approach (orange), percentage of highest classification rate for monomodal Raman approach (blue) and percentage of equal classification rates (yellow). (b) Corresponding averaged improvement of classification rates for multimodal data compared to monomodal IR data (orange) and compared to monomodal Raman data (blue). (For interpretation of the references to color in this figure legend, the reader is referred to the Web version of this article.)

respectively. Compared to the Raman method, classification rates increased by 7.6 ± 0.7% and training accuracy by 7.8 ± 0.8% on average. In comparison to the IR method, the mean percentage improvement in classification rate was 2.1 ± 0.3% and that of training accuracy 3.0 ± 0.4%. 9.5% of the classification setups resulted in a higher accuracy for the classification of monomodal IR data. A detailed representation of all classification rates is shown in Table 1 and Table 2.

We furthermore subdivided the results of improved classification rates into different classes according to their degree of improvement and evaluated the corresponding distribution. We differentiated between

Table 1
Classification results for the considered classification setups of PS1. The highest classification rate for the considered setup is colored according to its approach: Multimodal (MM - *green*), IR (IR - *orange*) and Raman (Ra - *blue*).

LDA

	Subs2			SubS5			Rand5			Rand15			Rand25			Rand35			Rand45		
Feature	IR	Ra	MM	IR	Ra	MM	IR	Ra	MM	IR	Ra	MM	IR	Ra	MM	IR	Ra	MM	IR	Ra	MM
PCA3	79.80%	85.92%	96.57%	80.23%	86.68%	96.53%	71.00%	79.29%	92.37%	75.37%	82.23%	95.03%	76.09%	82.63%	95.57%	76.42%	82.74%	95.79%	76.52%	82.83%	95.91%
PCA5	89.27%	91.43%	96.86%	89.31%	91.33%	97.12%	79.76%	84.08%	89.55%	85.46%	86.06%	94.79%	86.52%	86.41%	95.48%	86.44%	86.37%	95.85%	86.68%	86.37%	95.83%
PCA10	91.39%	91.96%	97.22%	90.79%	91.30%	97.47%	73.96%	81.88%	70.32%	84.52%	86.83%	94.56%	85.22%	87.48%	95.84%	85.73%	87.90%	96.37%	86.31%	87.70%	96.61%
MNF10	90.94%	91.63%	97.18%	90.38%	91.73%	96.99%	72.41%	80.88%	66.57%	84.44%	86.80%	94.52%	86.04%	87.46%	95.49%	86.93%	87.29%	96.18%	87.52%	87.62%	96.38%
MNF20	92.90%	93.02%	97.76%	92.19%	92.68%	97.37%	51.19%	59.42%	65.69%	81.29%	87.21%	91.38%	85.05%	88.20%	94.81%	86.64%	88.35%	95.74%	87.40%	88.58%	96.21%
MNF30	93.47%	92.73%	97.76%	92.81%	92.02%	97.42%	51.49%	58.84%	56.22%	78.99%	86.02%	84.51%	83.89%	87.96%	92.90%	84.96%	88.42%	94.58%	86.72%	88.53%	95.64%
LDA2	89.96%	74.37%	97.39%	81.53%	67.17%	95.77%	90.82%	70.91%	98.31%	92.50%	74.70%	98.53%	92.72%	75.05%	98.54%	93.10%	75.06%	98.58%	93.13%	75.39%	98.61%
LDA4	94.24%	92.57%	97.63%	90.82%	82.07%	96.02%	95.59%	94.43%	98.31%	96.25%	95.36%	98.63%	96.37%	95.48%	98.65%	96.42%	95.55%	98.67%	96.46%	95.55%	98.68%
LDA6	95.47%	92.78%	97.88%	92.45%	86.81%	96.28%	96.15%	93.99%	97.69%	97.01%	95.28%	98.71%	97.10%	95.47%	98.74%	97.13%	95.39%	98.76%	97.17%	95.41%	98.77%

SVM

	Subs2			SubS5			Rand5			Rand15			Rand25			Rand35			Rand45		
Feature	IR	Ra	MM	IR	Ra	MM	IR	Ra	MM	IR	Ra	MM	IR	Ra	MM	IR	Ra	MM	IR	Ra	MM
PCA3	87.18%	91.51%	98.00%	85.18%	89.06%	96.48%	62.48%	70.22%	77.33%	71.30%	78.22%	88.81%	74.66%	81.79%	91.94%	76.49%	84.07%	93.45%	77.52%	85.56%	94.35%
PCA5	95.51%	95.47%	98.08%	92.86%	94.16%	96.76%	65.33%	73.94%	77.05%	78.15%	83.66%	88.77%	82.93%	87.96%	92.43%	86.05%	90.43%	94.20%	87.20%	90.84%	94.83%
PCA10	96.78%	95.55%	98.12%	94.41%	94.06%	96.66%	64.52%	73.34%	74.14%	82.68%	84.58%	89.86%	87.50%	88.20%	93.13%	89.70%	90.31%	94.63%	91.08%	91.19%	95.42%
MNF10	96.04%	95.59%	97.63%	94.16%	94.80%	97.09%	71.15%	75.09%	77.12%	82.12%	84.60%	88.89%	86.83%	87.39%	91.64%	88.97%	89.39%	93.36%	90.38%	90.53%	94.60%
MNF20	97.27%	95.92%	97.76%	94.72%	94.57%	97.02%	69.97%	72.29%	76.42%	83.77%	84.58%	89.07%	88.77%	88.31%	91.96%	90.51%	89.65%	93.61%	91.61%	90.59%	94.49%
MNF30	97.10%	95.96%	98.00%	95.15%	94.03%	97.09%	67.87%	71.63%	75.36%	84.19%	84.00%	89.13%	88.33%	87.69%	92.20%	90.45%	89.44%	93.41%	92.05%	90.68%	94.51%
LDA2	89.67%	74.49%	97.18%	79.34%	65.99%	93.27%	79.19%	64.61%	84.85%	84.63%	68.33%	93.95%	85.87%	69.10%	95.68%	87.10%	70.22%	96.39%	88.11%	70.21%	96.38%
LDA4	94.86%	93.18%	97.51%	87.37%	73.44%	89.59%	87.10%	80.26%	87.65%	91.35%	88.69%	94.29%	92.56%	91.12%	96.05%	93.79%	92.58%	96.82%	94.41%	93.76%	97.17%
LDA6	95.63%	93.02%	97.27%	87.27%	77.86%	89.41%	88.19%	80.47%	86.18%	92.66%	89.81%	94.18%	93.84%	92.07%	96.08%	94.75%	93.11%	96.85%	95.09%	94.10%	97.38%

NBC

	Subs2			SubS5			Rand5			Rand15			Rand25			Rand35			Rand45		
Feature	IR	Ra	MM	IR	Ra	MM	IR	Ra	MM	IR	Ra	MM	IR	Ra	MM	IR	Ra	MM	IR	Ra	MM
PCA3	82.00%	85.67%	96.12%	81.56%	84.97%	95.87%	67.82%	75.34%	83.47%	73.53%	81.75%	92.14%	74.05%	82.56%	93.61%	73.72%	82.86%	94.58%	73.64%	83.21%	95.07%
PCA5	89.27%	88.65%	96.24%	88.93%	89.16%	95.97%	71.71%	77.31%	82.04%	81.22%	85.10%	91.88%	83.15%	86.43%	94.16%	84.20%	86.93%	94.76%	84.71%	87.20%	94.94%
PCA10	88.53%	89.47%	96.86%	89.72%	89.59%	96.40%	70.56%	71.09%	76.76%	83.55%	84.07%	91.71%	84.78%	86.03%	93.67%	86.01%	86.86%	94.83%	86.56%	86.89%	95.33%
MNF10	89.55%	87.96%	95.51%	88.85%	88.62%	96.35%	66.44%	72.91%	78.38%	82.81%	85.37%	91.88%	85.15%	86.54%	93.54%	85.65%	86.73%	94.34%	86.66%	87.26%	95.15%
MNF20	89.71%	88.37%	96.37%	90.13%	88.34%	95.74%	61.15%	66.44%	72.89%	83.18%	84.33%	91.18%	85.86%	86.05%	93.48%	86.62%	86.88%	94.41%	87.16%	87.24%	94.96%
MNF30	89.39%	88.16%	95.31%	90.31%	87.19%	95.38%	60.31%	63.40%	70.10%	80.52%	82.88%	89.80%	83.67%	85.79%	92.82%	84.63%	86.30%	93.54%	85.51%	87.02%	94.04%
LDA2	89.27%	74.08%	96.78%	80.10%	65.20%	94.92%	80.52%	66.97%	92.88%	89.62%	73.10%	97.09%	90.67%	73.70%	97.53%	91.42%	74.67%	97.64%	91.71%	75.04%	97.80%
LDA4	93.63%	92.29%	96.65%	89.85%	78.32%	94.97%	88.27%	86.65%	93.41%	94.77%	93.47%	97.13%	95.52%	94.47%	97.52%	95.85%	94.68%	97.81%	95.98%	94.80%	97.73%
LDA6	93.80%	91.84%	96.45%	90.82%	81.94%	95.03%	86.08%	85.25%	91.05%	94.73%	93.61%	97.10%	95.16%	94.36%	97.50%	95.77%	94.58%	97.72%	95.94%	94.76%	97.81%

Table 2
Classification results for the considered classification setups of PS2. The highest classification rate for the considered setup is colored according to its approach: Multimodal (MM - *green*), IR (IR - *orange*)and Raman (Ra - *blue*).

LDA

	Subs2			SubS5			Rand5			Rand15			Rand25			Rand35			Rand45		
Feature	IR	Ra	MM	IR	Ra	MM	IR	Ra	MM	IR	Ra	MM	IR	Ra	MM	IR	Ra	MM	IR	Ra	MM
PCA3	89.43%	86.49%	92.82%	89.13%	86.58%	.32%	87.19%	77.31%	87.41%	89.67%	78.71%	90.40%	90.02%	81.84%	90.76%	90.45%	82.12%	91.08%	90.42%	83.24%	90.98%
PCA5	90.12%	89.31%	94.29%	89.72%	89.18%	93.90%	81.81%	76.84%	84.88%	86.21%	81.24%	91.18%	86.57%	84.04%	91.72%	87.58%	85.30%	92.27%	87.71%	85.93%	92.01%
PCA10	90.24%	90.12%	94.94%	89.34%	90.13%	94.34%	77.34%	76.64%	61.94%	84.52%	82.47%	91.25%	85.38%	84.86%	92.62%	85.74%	85.25%	93.08%	86.12%	85.56%	93.29%
MNF10	93.67%	90.49%	95.39%	92.50%	90.59%	94.49%	76.65%	75.68%	60.76%	86.12%	84.67%	90.79%	88.06%	86.34%	92.32%	88.60%	86.86%	93.20%	89.48%	87.30%	93.38%
MNF20	96.04%	90.33%	97.51%	94.77%	91.07%	96.45%	57.74%	56.17%	66.38%	86.77%	83.96%	88.33%	89.76%	86.33%	93.09%	91.46%	86.94%	94.36%	91.83%	87.20%	94.85%
MNF30	95.96%	91.51%	97.80%	94.69%	90.92%	96.51%	57.42%	58.16%	60.87%	86.43%	82.96%	81.30%	90.68%	86.46%	92.03%	91.77%	87.70%	93.93%	92.38%	88.09%	94.71%
LDA2	93.88%	89.02%	95.63%	88.67%	66.28%	84.49%	92.25%	79.54%	97.12%	94.02%	83.27%	97.55%	94.43%	84.95%	97.60%	94.53%	85.17%	97.68%	94.77%	85.72%	97.70%
LDA4	96.90%	93.47%	97.14%	95.87%	81.33%	92.12%	97.24%	94.30%	97.11%	97.89%	95.59%	98.21%	97.96%	95.85%	98.29%	98.03%	95.88%	98.32%	98.08%	96.00%	98.34%
LDA6	97.22%	93.80%	97.39%	96.02%	83.44%	93.78%	97.44%	94.81%	96.96%	97.95%	95.74%	98.26%	98.00%	95.84%	98.38%	98.03%	95.89%	98.40%	98.06%	95.90%	98.44%

SVM

	Subs2			SubS5			Rand5			Rand15			Rand25			Rand35			Rand45		
Feature	IR	Ra	MM	IR	Ra	MM	IR	Ra	MM	IR	Ra	MM	IR	Ra	MM	IR	Ra	MM	IR	Ra	MM
PCA3	96.69%	94.57%	97.80%	94.54%	90.13%	95.61%	78.92%	76.01%	82.35%	86.45%	84.09%	89.40%	89.45%	86.56%	91.81%	90.72%	88.09%	93.45%	91.61%	89.14%	93.79%
PCA5	97.67%	94.33%	.20%	96.02%	91.73%	96.79%	77.70%	72.51%	79.58%	87.79%	83.96%	90.48%	90.71%	87.21%	92.28%	92.60%	88.84%	94.20%	93.33%	90.03%	94.78%
PCA10	98.00%	95.10%	98.33%	96.84%	91.99%	97.30%	75.53%	72.55%	75.81%	88.38%	84.91%	90.75%	91.63%	88.87%	92.89%	93.07%	89.91%	94.63%	93.92%	90.93%	94.75%
MNF10	97.14%	95.14%	97.55%	95.56%	88.65%	96.79%	72.02%	70.95%	73.99%	84.60%	84.06%	88.21%	90.02%	87.25%	91.77%	92.26%	89.25%	93.36%	93.56%	90.03%	94.27%
MNF20	97.27%	95.14%	98.12%	96.51%	91.25%	96.84%	70.82%	69.69%	71.69%	85.68%	83.77%	88.96%	90.45%	87.45%	92.13%	92.40%	88.86%	93.61%	93.77%	90.25%	94.74%
MNF30	97.31%	94.69%	98.29%	96.28%	91.76%	96.63%	71.31%	67.14%	70.87%	86.13%	84.37%	89.70%	90.92%	87.76%	92.15%	92.50%	89.18%	93.41%	93.71%	90.05%	94.55%
LDA2	94.69%	88.61%	95.76%	87.35%	61.12%	75.74%	83.47%	67.19%	90.43%	86.65%	72.49%	93.49%	88.23%	73.89%	94.84%	88.68%	75.62%	96.39%	89.80%	77.16%	95.84%
LDA4	97.02%	92.94%	97.14%	93.52%	74.67%	83.98%	90.19%	84.10%	90.50%	92.85%	91.19%	94.33%	94.19%	92.24%	95.69%	95.04%	92.85%	96.82%	95.57%	93.61%	96.67%
LDA6	97.02%	91.59%	95.80%	92.02%	71.53%	82.30%	91.09%	85.95%	90.20%	94.41%	91.60%	94.27%	95.33%	92.40%	95.74%	95.48%	93.02%	96.85%	96.14%	93.68%	96.91%

NBC

	Subs2			SubS5			Rand5			Rand15			Rand25			Rand35			Rand45		
Feature	IR	Ra	MM	IR	Ra	MM	IR	Ra	MM	IR	Ra	MM	IR	Ra	MM	IR	Ra	MM	IR	Ra	MM
PCA3	92.09%	88.98%	92.68%	92.09%	88.98%	92.68%	79.00%	75.97%	81.85%	88.30%	81.13%	90.65%	89.58%	82.99%	91.87%	90.14%	83.64%	92.29%	90.60%	84.45%	92.78%
PCA5	93.80%	89.77%	94.57%	93.80%	89.77%	94.57%	78.74%	71.70%	81.09%	89.33%	77.27%	91.08%	90.63%	76.51%	92.70%	91.67%	77.34%	93.49%	91.82%	77.52%	93.55%
PCA10	93.09%	83.39%	94.08%	93.09%	83.39%	94.08%	78.11%	68.77%	78.96%	90.24%	76.84%	90.97%	91.93%	75.63%	92.69%	92.29%	76.81%	93.58%	92.54%	75.23%	93.61%
MNF10	91.48%	86.07%	92.35%	91.48%	86.07%	92.35%	73.01%	66.91%	75.81%	87.39%	73.82%	88.43%	89.67%	74.01%	90.52%	90.07%	73.19%	91.39%	90.27%	73.74%	91.78%
MNF20	91.28%	79.13%	93.14%	91.28%	79.13%	93.14%	68.95%	63.88%	71.95%	87.27%	74.51%	88.70%	90.10%	75.80%	90.84%	90.87%	76.32%	91.72%	91.24%	76.35%	92.25%
MNF30	89.29%	81.51%	92.30%	89.29%	81.51%	92.30%	66.05%	60.55%	68.82%	86.37%	72.38%	86.93%	88.89%	74.72%	90.23%	89.65%	73.72%	90.78%	90.03%	73.92%	91.34%
LDA2	89.90%	55.74%	76.07%	89.90%	55.74%	76.07%	84.43%	72.93%	88.99%	91.81%	81.19%	95.42%	93.23%	84.37%	96.22%	93.58%	85.00%	96.44%	93.94%	86.52%	96.59%
LDA4	95.05%	69.01%	84.03%	95.05%	69.01%	84.03%	88.72%	86.16%	90.95%	95.16%	93.29%	96.48%	96.00%	93.93%	97.35%	96.34%	94.52%	97.63%	96.56%	94.81%	97.76%
LDA6	95.82%	64.97%	81.38%	95.82%	64.97%	81.38%	89.11%	85.31%	90.87%	95.39%	93.28%	96.79%	96.34%	94.33%	97.44%	96.61%	94.83%	97.65%	96.67%	95.04%	97.80%

cases of *noticeable improvement* (0%–5%), *significant improvement* (5%–15%) and *remarkable improvement* (>15%). As presented in Fig. 4a and b, 184 of 189 individual classification setups led to improved classification rates with regard to PS1. In comparison to the classification of monomodal IR data, 63 setups resulted in a *noticeable improvement* in classification rates. The majority of 105 setups led to a *significant improvement* and 16 setups even led to a *remarkable improvement*. In comparison to the classification results of monomodal Raman data, 66 classification setups resulted in a *noticeable improvement* and 95 in a *significant improvement*. A *remarkable improvement* could be determined in 23 cases. For PS2, 171 of 189 classification setups led to improved classification rates. Fig. 4c and d shows that the results in comparison to the classification of monomodal IR data could be subdivided into 159 setups that resulted in a *noticeable improvement* and 12 setups that resulted in a *significant improvement*. In comparison to the Raman method, the classification of multimodal data resulted in a *noticeable improvement* for 67 cases and for 82 cases in a *significant improvements*. For 22 classification setups, a *remarkable improvement* could be achieved.

The results can be supported by taking the classification rates of PS1 as presented in Table 1 into account. In addition to the improvements in classification rates that have generally been achieved for the multimodal approach, the sensitivity of the results towards the composition of the classification setups is of interest. Here, the degree of classification improvement realized by consideration of multimodal data varies between less than 1% and more than 30%. For randomly chosen training data sets consisting of few feature vectors (Rand5 and Rand15), a high variation in classification results and thus a high sensitivity towards the chosen features could further be recognized. Exceptional cases exists where classification of monomodal data even resulted in a higher accuracy on average. Nevertheless, the clear majority of the considered classification setups led to numerical improvements after using concatenated features from both spectroscopic methods, emphasizing the

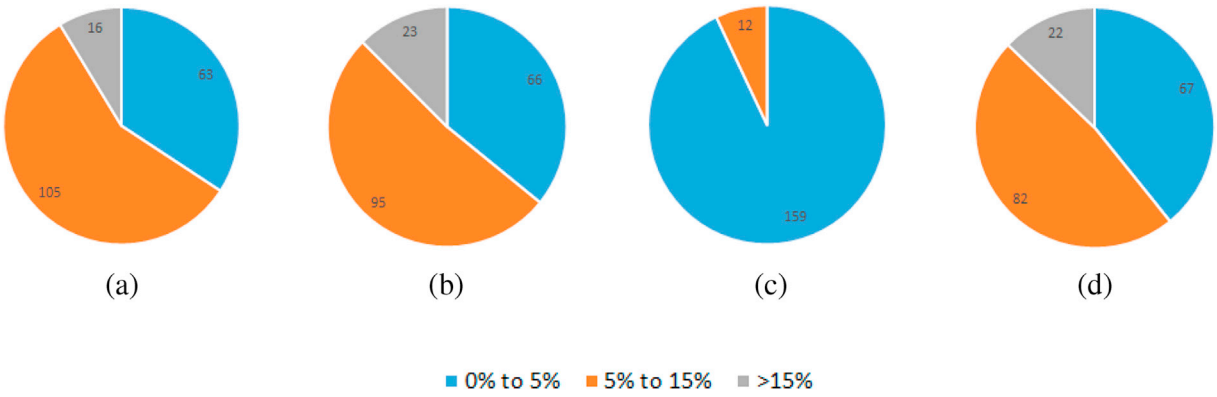

Fig. 4. Partitions of classification setups according to their degree of improvement (a) Partition for PS1 in comparison to the IR method (b) Partition for PS1 in comparison to the Raman method (c) Partition for S2 in comparison to the IR method. (d) Partition for PS2 in comparison to the Raman method.

potential of a multimodal approach. The results of PS2 presented in Table 2 can be interpreted similarly and show comparable outcomes. But even though the clear majority of setups resulted in a numerical improvement for classification of multimodal data, a considerable number of cases where only a marginal difference in classification rates could be determined should be pointed out. Especially the IR method shows good, in some cases even better results, compared to the multimodal approach, without any recognizable dependency on the training data sets or the dimensionality of the feature space.

A comparison of the class dependent results for classification of monomodal and multimodal data showed that all classes provided by PS1 generally have a higher sensitivity for the multimodal approach. As presented in Fig. 5a, a clear majority of at least 60% of all classification setups resulted in higher classification rates across the classes. Here, class

Fig. 5. Class dependent distribution of highest classification rates for all classification setups considering classification results for monomodal and multimodal data of PS1 (a) and PS2 (c). Percentage of improved classification rates by multimodal approach (green), percentage of highest classification rate for monomodal IR approach (orange), percentage of highest classification rate for monomodal Raman approach (blue) and percentage of equal classification rates (yellow). Averaged, class dependent improvement of classification rates for multimodal data compared to monomodal IR data (orange) and compared to monomodal Raman data (blue) PS1 (b) and PS2 (d). (For interpretation of the references to color in this figure legend, the reader is referred to the Web version of this article.)

membership assignments of the pixel vectors were done according to the reference image in Fig. 2d, where *Class 1* (SAN), *Class 3* (colorant), *Class 5* (PMMA) and *Class 7* (background) correspond to spectral signatures of pure material distributions, and *Class 2* (colorant/SAN), *Class 4* (colorant/PMMA) and *Class 6* (PMMA/SAN) to spectral signatures of mixed materials. Fig. 5b illustrates that *Class 2* and *Class 4* show a high averaged reduction in error rates. It should be noted that these classes represent mixed-material targets that are providing more complex spectral signatures. Comparable results could be achieved for PS2 and are presented in Fig. 5c and d, where class membership assignments of the pixel vectors were done according to the reference image in Fig. 2h, with *Class 1* (PMMA), *Class 3* (PS), *Class 5* (PEI) and *Class 7* (background) representing spectral signatures of pure material distributions, and *Class 2* (PMMA/PS), *Class 4* (PS/PEI) and *Class 6* (PEI/PMMA) representing spectral signatures of mixed materials. Here, the multimodal approach led to an improved classification rate for all processed sample components. Only *Class 7*, which represents the gold mirror background of the sample that does not provide a material specific spectral signature, resulted in more accurate classification rates for the monomodal IR data. Even here, the noticeable averaged reduction of the error rates concerning *Class 2*, *Class 4* and *Class 6*, representing mixed-material targets for PS2, could be observed.

4.3. Complementarity of features

The spectral data presented in Fig. 6 show exemplary that the monomodal feature vectors have the potential to complement each other meaningfully in terms of material-specific information content. The illustrated Raman and IR spectra show normalized spectral signatures of the polymers of PS1. In this example, PCA was applied for dimensionality reduction. Thus, a set of loading values has been obtained while determining each principal component, giving information about how the different variables contribute to the corresponding principle component. Since high loading values represent a high contribution of the corresponding variable, we marked the variables that provide the highest loading values for the determination of the first 3 principal components. For the IR spectra, it can be shown that these variables are assignable to material-specific peaks of only two different sample components. Consequently two variables of material-specific information content are of high influence in the corresponding classification approach. Here, an accurate classification of the spectral signatures might be challenging in the corresponding feature space, since three different components were used to prepare the sample. A similar situation occurred for the Raman spectra. Here, the variables are also assignable to material-specific peaks of only 2 different sample components. Furthermore, the variables with the greatest impact on the estimation of the first and the third principal component are identical. Hence, a successful classification of all spectral signatures on the basis of the first 3 principal components might become difficult. By concatenating the monomodal feature vectors, the corresponding feature space is extended in such a way that at least one material-specific variable from the IR or the Raman data is of high influence concerning the classification potential provided by the first 3 principal components of both spectroscopic data sets. Consequently, the extension of the feature space is considered to be meaningful in terms of material-specific spectral information content and not to be dominated by noisy or material-independent parts of the spectra. With regard to Table 1, the results of classification setups for PS1, considering the first 3 principal components (PCA3), support these assertions as well. The spectral data presented in Fig. 7 allow to discuss the difference between the results of PS1 and PS2. Analogous to the spectral data of PS1, normalized material-specific signatures of the sample components are shown and the variables with the highest impact on the principal components estimation are marked. With regard to the Raman spectra, two variables represent material-specific peaks of two components. The third variable can be assigned to a peak that is observable in the spectral signatures of all materials, only varying in its intensity. Hence, the classification of the materials by considering the first 3 principal components of the Raman spectra might be challenging. In contrast, the variables that

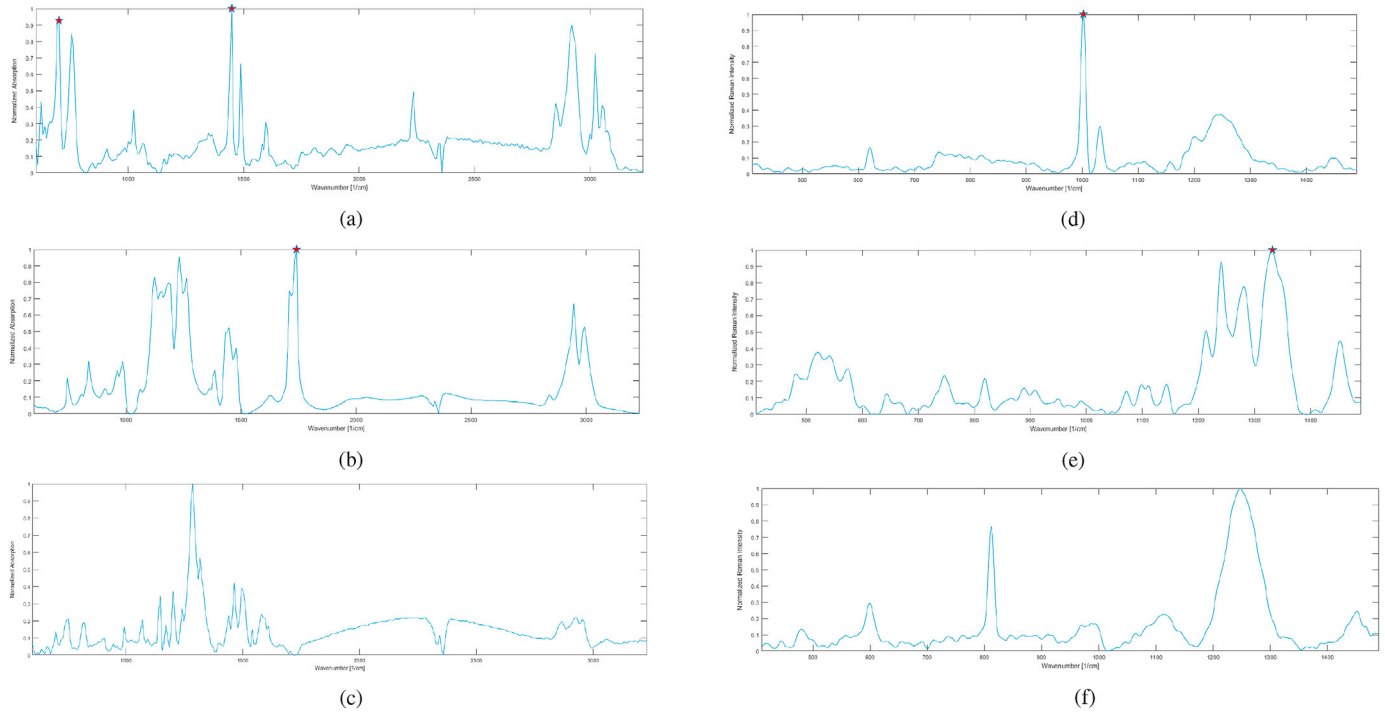

Fig. 6. Exemplary spectral signatures of pure material distributions for components of PS1. (a) IR spectrum of SAN, (b) Raman spectrum of SAN, (c) IR spectrum of PMMA, (d) Raman spectrum of PMMA, (e) IR spectrum of black colorant, (f) Raman spectrum of black colorant. The red stars mark the variables with highest loading value concerning the determination of the first 3 principal components and thus, represent the variables with the highest influence on the first 3 principal components computation. (For interpretation of the references to color in this figure legend, the reader is referred to the Web version of this article.)

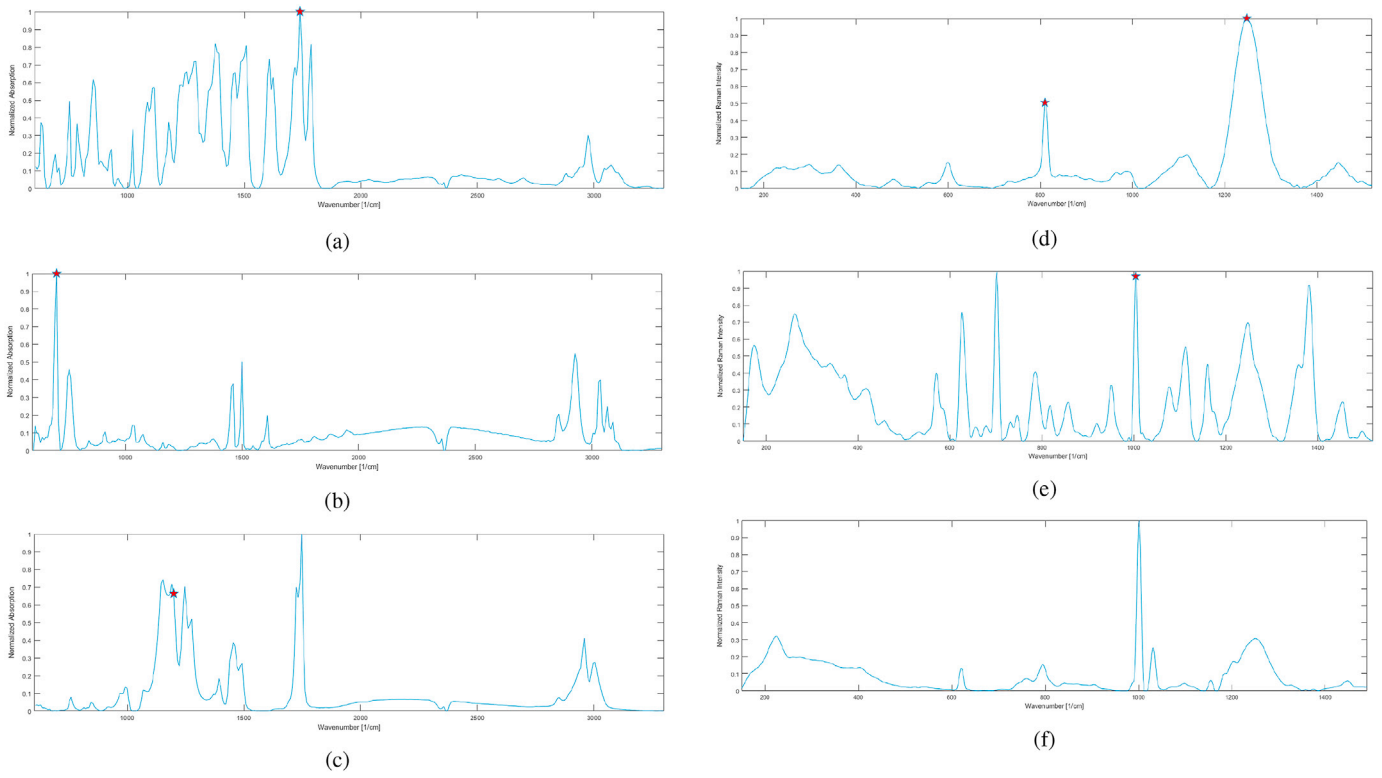

Fig. 7. Exemplary spectral signatures of pure material distributions for components of PS2. (a) IR spectrum of PEI, (b) Raman spectrum of PEI, (c) IR spectrum of PMMA, (d) Raman spectrum of PMMA, (e) IR spectrum of PS, (f) Raman spectrum of PS. The red stars mark the variables with highest loading value concerning the determination of the first 3 principal components and thus, represent the variables with the highest influence on the first 3 principal components computation. (For interpretation of the references to color in this figure legend, the reader is referred to the Web version of this article.)

were determined for the IR spectra can be assigned to different material-specific peaks, each representing one of the sample components. Consequently, the spectral signatures generated by the IR method provide a greater potential for a satisfying discrimination in the feature space defined by the first 3 principal components. The constantly high classification rates for PS2 with regard to the IR data support this assumption. Nevertheless, an extension of the feature space by features derived from the complementary spectroscopic approach led to improved classification rates for PS2, emphasizing that considering additional spectral information is beneficial in classification tasks, even for monomodal spectral signatures with high discrimination power.

5. Conclusions

The objective of the investigation presented in this contribution was to show that multimodal data derived from Raman and IR microspectroscopy contains complementary information that has the potential to improve the classification rates of hyperspectral material signatures, compared to the monomodal classification approaches. We have furthermore assumed that the complementarity is especially helpful in cases of challenging classification tasks, where a certain degree of data complexity is given. Within the scope of this contribution, data complexity was increased by rapid raster measurements of multiclass polymer samples, providing classification targets of pure and mixed materials. It could be shown that a feature-level fusion of information, extracted by statistic-based DR techniques, led to a numerical improvement for a clear majority of different classification setups, varying in features, training data and classification models. The results indicate that features derived from both spectroscopic approaches complement the feature space for classification tasks in a meaningful way.

We conclude that the benefit of applying a multimodal approach in vibrational microspectroscopy could successfully be demonstrated, especially by exemplary emphasizing a meaningful extension of the feature space. In addition, it could be demonstrated that the results depend on the choice of features, classification models and training data sets. Although the presented results give a promising indication of the impact of a multimodal vibrational microspectroscopic approach, it has to be stated that these conclusions are based on the analysis of artificially generated samples. Thus, the components that have been used to prepare the microscopic samples are of materials that provide a high activity and good spectral discriminative properties for both measurement concepts. For the different fields of research where vibrational microspectroscopy is of importance, a multimodal concept of Raman and IR approaches still has to prove itself. Nevertheless, in accordance with [9], the results presented in this contribution strongly support the concept of a multimodal approach in vibrational microspectroscopy and its application as an advanced method for challenging analytical and classification tasks.

Declarations of interest

None.

Acknowledgment

This work was funded by the German Research Foundation (DFG) as part of the research training group GRK 1564 ”Imaging New Modalities”. We further acknowledge the doctoral scholarship provided by the Department of Computer Science at the Hochschule Bonn-Rhein-Sieg University of Applied Sciences.

Appendix A. Supplementary data

Supplementary data to this article can be found online at https://doi.org/10.1016/j.chemolab.2018.11.013.

References

[1] C.C. Aggarwal, Data Classification: Algorithms and Applications, first ed., Chapman & Hall/CRC, 2014.

[2] C.M. Bishop, Pattern Recognition and Machine Learning (Information Science and Statistics), Springer-Verlag, Berlin, Heidelberg, 2006.

[3] C.-I. Chang, Appendix: algorithm compendium, in: Hyperspectral Data Processing, Wiley-Blackwell, 2013a, pp. 997–1051.

[4] C.-I. Chang, Data dimensionality reduction, in: Hyperspectral Data Processing, Wiley-Blackwell, 2013b, pp. 168–199.

[5] F.C. Clarke, M.J. Jamieson, D.A. Clark, S.V. Hammond, R.D. Jee, A.C. Moffat, Chemical image fusion. the synergy of ft-nir and Raman mapping microscopy to enable a more complete visualization of pharmaceutical formulations, Anal. Chem. 73 (10) (2001) 2213–2220.

[6] W.S. Cleveland, Robust locally weighted regression and smoothing scatterplots, J. Am. Stat. Assoc. 74 (368) (1979) 829–836.

[7] M. Diem, et al., Applications of infrared and Raman microspectroscopy of cells and tissue in medical diagnostics: present status and future promise, Spectros. Int. J. 27 (5–6) (2012) 463–496.

[8] C. Gendrin, Y. Roggo, C. Collet, Pharmaceutical applications of vibrational chemical imaging and chemometrics: a review, J. Pharmaceut. Biomed. Anal. 48 (3) (2008) 533–553.

[9] A.A. Gowen, R.M. Dorrepaal, Multivariate chemical image fusion of vibrational spectroscopic imaging modalities, Molecules 21 (7) (2016).

[10] H. Gremlich, B. Yan, Infrared and Raman Spectroscopy of Biological Materials. Practical Spectroscopy, Taylor & Francis, 2000.

[11] I. Jolliffe, Principal Component Analysis. Singer Series in Statistics, Springer, 2002.

[12] A. Käppler, D. Fischer, S. Oberbeckmann, G. Schernewski, M. Labrenz, K.-J. Eichhorn, B. Voit, Analysis of environmental microplastics by vibrational microspectroscopy: ftir, Raman or both? Anal. Bioanal. Chem. 408 (29) (2016) 8377–8391.

[13] J. Katon, Applications of vibrational microspectroscopy to chemistry, Vib. Spectrosc. 7 (3) (1994) 201–229.

[14] J.L. Koenig, J.P. Bobiak, Raman and infrared imaging of dynamic polymer systems, Macromol. Mater. Eng. 292 (7) (2007) 801–816.

[15] C. Krafft, D. Codrich, G. Pelizzo, V. Sergo, Raman and ftir microscopic imaging of colon tissue: a comparative study, J. Biophot. 1 (2) (2008) 154–169.

[16] C. Krafft, S.B. Sobottka, G. Schackert, R. Salzer, Raman and infrared spectroscopic mapping of human primary intracranial tumors: a comparative study, J. Raman Spectrosc. 37 (1–3) (2006) 367–375.

[17] D. Lahat, T. Adali, C. Jutten, Multimodal data fusion: an overview of methods, challenges, and prospects, Proc. IEEE 103 (9) (Sept 2015) 1449–1477.

[18] P. Larkin, Chapter 1-introduction: infrared and Raman spectroscopy, in: Infrared and Raman Spectroscopy, Elsevier, Oxford, 2011a, pp. 1–5.

[19] P. Larkin, Chapter 2-basic principles, in: Infrared and Raman Spectroscopy, Elsevier, Oxford, 2011b, pp. 7–25.

[20] S.-Y. Lin, M.-J. Li, W.-T. Cheng, Ft-ir and Raman vibrational microspectroscopies used for spectral biodiagnosis of human tissues, Spectroscopy 21 (1) (2007) 1–30.

[21] L.V.D. Maaten, E. Postma, J.V.D. Herik, Dimensionality Reduction: a Comparative Review. Tech. Rep, Tilburg University Technical Report, 2009.

[22] M.J. Pelletier, C.C. Pelletier, Spectroscopic theory for chemical imaging, in: Raman, Infrared, and NearInfrared Chemical Imaging, Wiley-Blackwell, 2011, pp. 1–20.

[23] J. Peng, S. Peng, A. Jiang, J. Wei, C. Li, J. Tan, Asymmetric least squares for multiple spectra baseline correction, Anal. Chim. Acta 683 (1) (2010) 63–68.

[24] D. Perez-Guaita, K. Kochan, M. Martin, D.W. Andrew, P. Heraud, J.S. Richards, B.R. Wood, Multimodal vibrational imaging of cells, Vib. Spectrosc. 91 (Supplement C) (2017) 46–58.

[25] P.-Y. Sacr, C.D. Bleye, P.-F. Chavez, L. Netchacovitch, P. Hubert, E. Ziemons, Data processing of vibrational chemical imaging for pharmaceutical applications, J. Pharmaceut. Biomed. Anal. 101 (2014) 123–140.

[26] E. Smith, G. Dent, Modern Raman Spectroscopy: a Practical Approach, Wiley, 2005.

[27] L.G. Thygesen, M.M. Lkke, E. Micklander, S.B. Engelsen, Vibrational microspectroscopy of food. Raman vs. ft-ir, Trends Food Sci. Technol. 14 (1) (2003) 50–57.